Chinese Chemical Letters 35 (2024) 109453

Contents lists available at ScienceDirect

Chinese Chemical Letters

journal homepage: www.elsevier.com/locate/cclet

Covalently bonded ternary photocatalyst comprising $MoSe_2$/black phosphorus nanosheet/graphitic carbon nitride for efficient moxifloxacin degradation

Yuhao Ma[a,b], Yufei Zhou[a,*], Mingchuan Yu[a], Cheng Fang[c], Shaoxia Yang[b], Junfeng Niu[a]

[a] College of Environmental Science and Engineering, North China Electric Power University, Beijing 102206, China
[b] College of Water Conservancy and Hydropower Engineering, North China Electric Power University, Beijing 102206, China
[c] Global Centre for Environmental Remediation (GCER), University of Newcastle, Callaghan, NSW 2308, Australia

ARTICLE INFO

Article history:
Received 2 September 2023
Revised 5 December 2023
Accepted 22 December 2023
Available online 30 December 2023

Keywords:
Ternary heterojunction
Black phosphorus nanosheets
Covalent bond
Photocatalytic degradation
Graphitic carbon nitride

ABSTRACT

Covalently bonded bridging between different semiconductors is a remarkable approach to improve the transfer of charge carriers at interfaces. In this study, we designed a ternary heterojunction (MBG) combining of molybdenum diselenide ($MoSe_2$), black phosphorus nanosheets (Bpn) and graphitic carbon nitride (GCN). Among this MBG of $MoSe_2$/Bpn/GCN, (i) the covalently bonded bridging effect between Bpn/GCN facilitates directional charge carrier transfer, meanwhile (ii) a Z-scheme heterojunction is formed between $MoSe_2$/GCN to enhance the separation of photogenerated carriers. Furthermore, (iii) this composite exhibits an increased absorption for visible light. Using this MBG, photocatalytic degradation of over 98% of moxifloxacin is achieved within 20 min, with $O_2^{\bullet-}$ confirmed as the primary photocatalytic active species. These findings provide novel insights into the construction of efficient heterojunction by covalently bonded bridging.

© 2024 Published by Elsevier B.V. on behalf of Chinese Chemical Society and Institute of Materia Medica, Chinese Academy of Medical Sciences.

The escalating global population has led to the wide use of antibacterial medicines in aquaculture, animal husbandry, and healthcare [1,2]. Among these medicines, moxifloxacin (MOX), classified as a fluoroquinolone, garners significant attention due to its remarkable antimicrobial activity against a broad spectrum of microorganisms, including Gram-positive, Gram-negative, anaerobic, and atypical strains [3–5]. However, MOX exhibits poor degradation within the animal body, resulting in the majority of the compound being excreted in its unaltered form [6]. Once arriving at the wastewater treatment plants, conventional treatment processes commonly encounter challenges in effectively degrading MOX, leading to the release of MOX, posing substantial ecological risks and threats to human health [7,8]. Therefore, it is crucial to find suitable treatment to remove MOX from wastewater. Currently, among various water treatment technologies [9,10], photocatalysis has gained much attention as it can use economic solar energy and exhibit high removal efficiency of fluoroquinolones [11–13].

In photocatalytic process, the property of the photocatalysts play a crucial role in determining the photocatalytic efficiency [14]. Metal-free graphitic carbon nitride (g-C_3N_4), with its non-toxicity, suitable band structure and stable physicochemical properties [15], is considered a potential material for photocatalytic treatment of wastewater, compared to metal oxygen/sulfide semiconductor materials such as titanium oxide (TiO_2) and chromium sulfide (CrS) [16–19]. However, the photocatalytic performance of g-C_3N_4 needs improvement due to its poor inherent conductivity and high recombination of photogenerated electron-hole pairs [20,21]. Unfortunately, the traditional modified approach may cause undesirable π-π stacking during synthesis, hindering the separation of photogenerated carries [22]. Previous research suggests that heterojunction construction by loading other semiconductor materials onto g-C_3N_4 is a feasible approach [23,24]. Recent studies have found that metal selenides are superior to metal sulfurs/oxides in conductivity due to the certain metallicity of selenium (Se) element [25,26]. Molybdenum diselenide ($MoSe_2$), for instance, possesses a narrow band gap that enables efficient absorption of a broad range of sunlight. Previous studies have found that $MoSe_2$ can serve as a reservoir for photogenerated electrons in heterojunction photocatalysts [27,28], with its energy band position well-suited for reducing dissolved oxygen in water and generating free radicals [29]. For example, in order to enhance the photogenerated carrier separation efficiency of g-C_3N_4, Zhang *et al.* synthesized an all-solid Ag_3PO_4/g-C_3N_4/$MoSe_2$ ternary photocatalyst. Herein, $MoSe_2$ plays

* Corresponding author.
E-mail address: zhouyf@ncepu.edu.cn (Y. Zhou).

https://doi.org/10.1016/j.cclet.2023.109453
1001-8417/© 2024 Published by Elsevier B.V. on behalf of Chinese Chemical Society and Institute of Materia Medica, Chinese Academy of Medical Sciences.

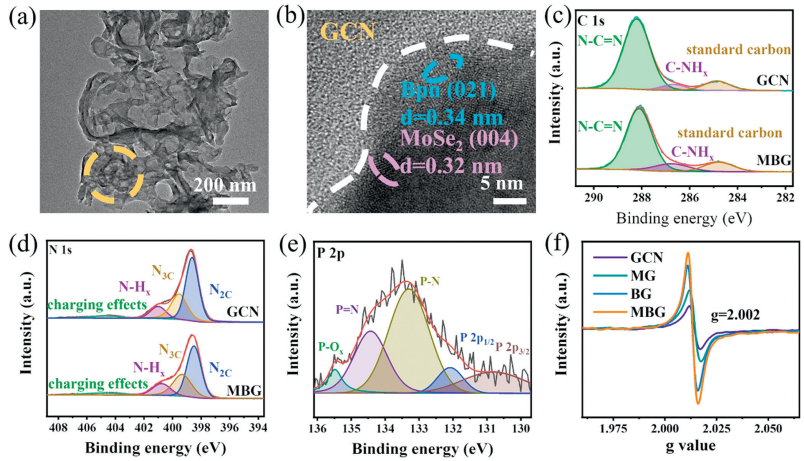

Fig. 1. (a) TEM image and (b) HRTEM image of MBG, (c) C 1s and (d) N 1s XPS spectra of GCN and MGB, (e) P 2p XPS spectrum of MBG, (f) ESR spectra of GCN, MG, BG and MBG.

a critical role as the electron transfer mediator, facilitating rapid electron migration between heterojunctions [30]. Similarly, black phosphorus nanosheets (Bpn) can serve as cocatalysts to modify g-C_3N_4 substrate due to their tunable energy band structure, fast charge transfer and broad light absorption ability. The formation of heterojunctions can regulate the electronic band structure on the surface of the complex, enhance the light absorption ability and photogenerated charge separation [31–33]. However, the loading black phosphorus through van der Waals force or electrostatic interaction cannot provide a direct interface contact, resulting in larger energy barriers for charge transfer between heterojunction interface [34,35]. Therefore, it is crucial to design an effective pathway for interface charge transfer across the heterojunctions.

In this study, we employed a pre-polymerizing method to synthesize g-C_3N_4 and successfully constructed g-C_3N_4-based ternary heterojunctions that are rich in N-vacancies (Supporting information). Material characterization revealed that Bpn was directly connected to N atoms in g-C_3N_4 (GCN) through a P-bridging, forming N-vacancies, promoting visible light absorption and charge carrier transfer at the heterojunction interfaces. Simultaneously, a Z-scheme heterojunction was formed between $MoSe_2$ and GCN, enhancing the separation of photogenerated carriers. Consequently, the degradation performance of this ternary composite, $MoSe_2$/Bpn/GCN (MBG), for MOX was significantly improved under the visible light irradiation. Finally, the mechanism of photoinduced MOX degradation by MBG was elucidated.

The morphology and structure of MBG nanocomposites were investigated by transmission electron microscopy (TEM) and high-resolution transmission electron microscopy (HRTEM). Fig. 1a depicts a three-dimensional coral-like porous structure of MBG, which can facilitate the interaction between the substrate and the active sites on the photocatalyst surface during catalysis. Fourier transform infrared spectroscopy (FTIR) results (Fig. S1 in Supporting information) reveal the presence of a typical broad peak ranging from 1200 cm^{-1} to 1700 cm^{-1}, corresponding to the stretching modes of C–N and C=N heterocycles [36]. Additionally, the intense peak at 810 cm^{-1} is attributed to the tri-s-triazine ring mode [37]. Similar absorption peaks observed in all samples suggest the preservation of the basic framework of GCN during the synthesis process. HRTEM image presented in Fig. 1b displays that lattice stripes with spacing of 0.32 nm and 0.34 nm, corresponding to $MoSe_2$ (004) crystal plane and Bpn (021) crystal plane, respectively [18,38]. This observation confirms the successful construction of a ternary heterojunction comprising $MoSe_2$, Bpn and GCN. Furthermore, Fig. S2 (Supporting information) demonstrates the uniform distribution of C, N, Mo, Se, P elements in the energy dispersive x-ray spectroscopy (EDS) elements mapping images. The morphology and structure of MBG nanocomposites have significant implications for their potential applications in photocatalysis.

X-ray photoelectron spectroscopy (XPS) was employed to determine the elemental composition and surface chemical state of the composites. Fig. S3 (Supporting information) exhibits the elemental spectra of GCN and MBG, displaying clear peaks of C, N and O. Nearly no signal of Mo, Se, and P is observed due to their low concentrations in the samples. In C 1s XPS spectra (Fig. 1c), the peaks at 288.2, 286.6 and 284.8 eV in both GCN and MBG correspond to N–C=N in the GCN framework, NH_x (x = 1, 2) at the edge of heptazine unit, and standard C–C, respectively [39]. Similarly, in N 1s XPS spectra (Fig. 1d), MBG exhibits peaks similar to those of GCN, where the peaks at 398.5, 399.5, 401.0 and 404.5 eV are attributed to C–N=C (N_{2C}), tricoordinate nitrogen (N_{3C}), amino group ($N-H_x$) and positively charged heterocycle, respectively [40]. As shown in Fig. S4 (Supporting information), the peaks of 130.5 eV, 131.3 eV and 135.2 eV correspond to P $2p_{3/2}$, P $2p_{1/2}$ and oxidized phosphorus of the P element in Bpn, respectively. Similarly, the peaks of P $2p_{3/2}$ and P $2p_{1/2}$ are located at the same position in MBG (Fig. 1e), implying the basic composition of Bpn in MBG is maintained. The peaks at 133.3 and 134.4 eV represent P–N and P=N bonds, respectively, indicating that Bpn is connected to GCN through a P-bridging [18,41]. Furthermore, the presence of electron spin resonance (ESR) signals at g = 2.002 in Fig. 1f indicates the existence of N-vacancies resulting from the surface defects of N in GCN. The ESR signal of N vacancies in MBG is stronger than those in Bpn/GCN (BG), $MoSe_2$/GCN (MG) and GCN, revealing the formation of abound covalent bonds when the heterostructure involving GCN, $MoSe_2$ and Bpn is constructed [42,43]. The N-vacancies can effectively adjust the band structure of g-C_3N_4, improve the ability of visible light capture, and increase the number of surface-active sites, thereby improving the photocatalytic performance [44,45].

As shown in Fig. 2a, the photocatalytic degradation of MOX by MBG was significantly enhanced compared with GCN, MG and BG. The optimal photocatalytic activity of MBG was observed when the addition of $MoSe_2$ and Bpn was 5 mg and 10 mg, respectively (Figs. S5a and b in Supporting information). Over 98% of MOX are removed in water under visible light irradiation within 20 min by MBG, whereas GCN only achieves ~31%. Furthermore, the *pseudo*-first-order kinetics curves (Fig. 2b) illustrate the relative photocatalytic degradation activity as follows: MBG > MG > BG > GCN, and the reaction rate constant of MBG (~0.196 min^{-1}) is about 6.3 times than that of pure GCN (~0.031 min^{-1}). This remarkable im-

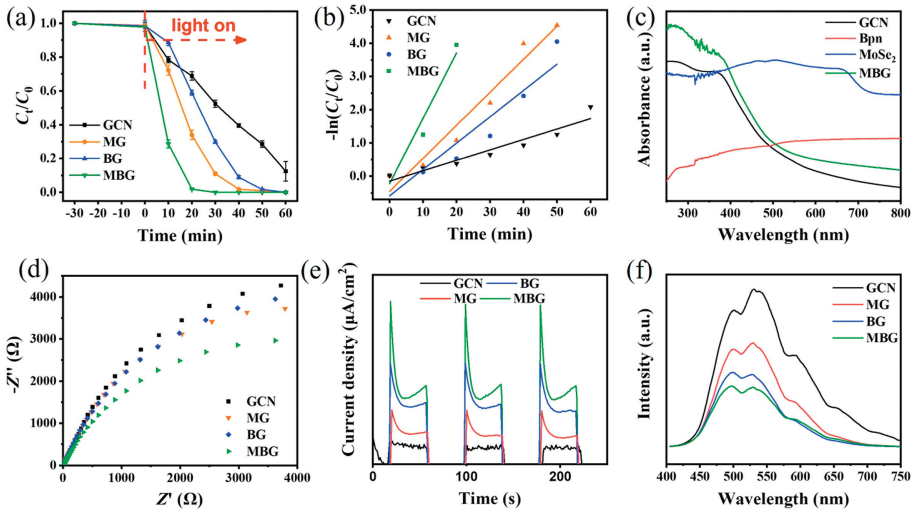

Fig. 2. (a, b) Photocatalytic performance and corresponding first-order kinetics curves of prepared photocatalysts. (c) UV–vis diffuse reflectance spectra (DRS) of $MoSe_2$, Bpn, GCN and MBG, (d) EIS spectra of GCN, MG, BG and MBG, (e) photocurrent response of GCN, MG, BG and MBG, (f) PL spectra of GCN, MG, BG and MBG.

provement in photocatalytic degradation indicates the formation of heterojunction structure among $MoSe_2$, Bpn and GCN, rather than a simple physical mixture. Compared to previously reported photocatalysts (Table S1 in Supporting information), the synthesized MBG presents higher efficiency for MOX degradation under visible light with lower catalyst dosage (0.2 g/L). Besides, the total organic carbon (TOC) removal of MOX is 42.5% in 120 min. The analysis conducted using an inductive coupled plasma emission spectrometer (ICP) reveals an absence of detectable quantities of the Mo element, indicating that metal leaching is negligible in the solution. Furthermore, to assess the reusability of MBG, we conducted cycle experiments. After 10 photocatalytic experiments (Fig. S6 in Supporting information), MGB remains higher photocatalytic efficiency, indicating its excellent stability.

The optical characterization of the material reveals that the addition of Bpn and $MoSe_2$ causes a red-shift the absorption edge of MBG relative to GCN, enhancing the absorption of MBG in the visible light range, as shown in Fig. 2c. Moreover, Kubelka-Munk function plot (Fig. S7 in Supporting information) reveals that the band gaps (E_g) of GCN, Bpn, and $MoSe_2$ are calculated to be ~2.66, ~0.70 and ~1.58 eV, respectively [46,47]. The semiconductor material charge transport properties were observed by electrochemical impedance spectroscopy (EIS). The Nyquist arc radius of MBG in Fig. 2d shrinks, indicating that the loading of $MoSe_2$ and Bpn on the GCN can benefit the effective transfer and separation of photogenerated carriers. Furthermore, the transient photocurrent response of the samples was determined under the irradiation of visible light. As shown in Fig. 2e, the current density generated by the ternary heterojunction MBG is significantly higher than that of GCN, indicating that MBG can increase the light absorption ability and reduces the re-combination of photogenerated carriers. This observation is further supported by photoluminescence (PL) spectra (Fig. 2f), where MBG presents the lowest signal intensity among the samples. The aforementioned photoelectron-performance proves that introduction of Bpn and $MoSe_2$ into GCN can improve the absorption of visible light. In addition, due to the excellent conductivity of Bpn and $MoSe_2$, the electron transfer ability of the ternary heterojunctions is improved. More importantly, the formation of heterojunctions restricts the recombination of photogenerated charges, ultimately improving the photocatalytic performance.

To determine the active components generated during photocatalysis, various active trapping agents were employed, including

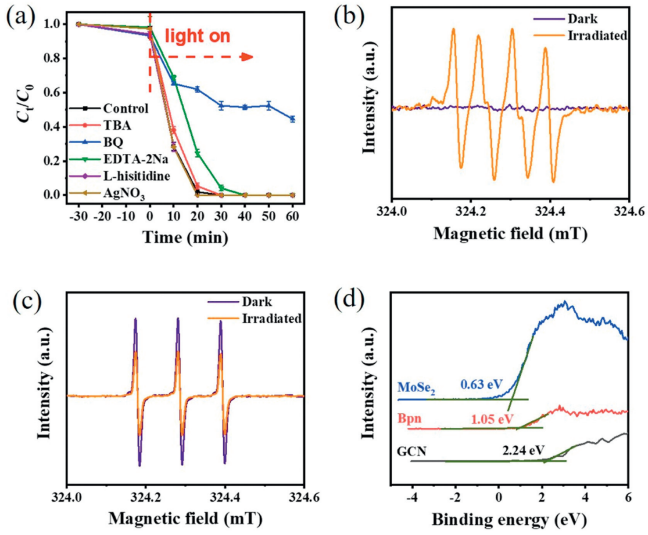

Fig. 3. (a) Photocatalytic trapping experiments. (b, c) ESR spectra of DMPO–$O_2^{\bullet-}$ and TEMPO-h^+. (d) valence band (VB) XPS spectra of GCN, Bpn and $MoSe_2$.

isopropanol (IPA), p-benzoquinone (BQ), disodium edetate (EDTA-2Na), L-histidine, and $AgNO_3$, which act as active traps for hydroxyl radical ($^{\bullet}OH$), superoxide radical ($O_2^{\bullet-}$), hole (h^+), singlet oxygen ($^1O_2$), and electron (e^-), respectively. As shown in Fig. 3a, the inhibitory effect of BQ on the photocatalytic degradation of MOX suggests the crucial involvement of $O_2^{\bullet-}$ in the photocatalytic degradation. Moreover, the characteristic signals in the ESR spectra in Figs. 3b and c obviously changes under the light irradiation, confirming that these active species are formed over MBG. The basic reaction formulas (Eqs. S1-S4 in Supporting information) involved are shown in the Supporting information [48,49]. Additionally, to clarify the energy band structures of the three semiconductors, the valence band (VB) values of GCN, Bpn, and $MoSe_2$ were obtained based on the VB XPS spectra, respectively. As illustrated in Fig. 3d, the VB values of GCN, Bpn and $MoSe_2$ are ~2.24, ~1.05 and ~0.63 eV, respectively. By employing the calculation formula: $E_g = E_{VB} - E_{CB}$, the conduction band (CB) values of GCN, Bpn, and $MoSe_2$ were determined to be −0.42, 0.35, and −0.95 eV, respectively. These results provide valuable insights into the active

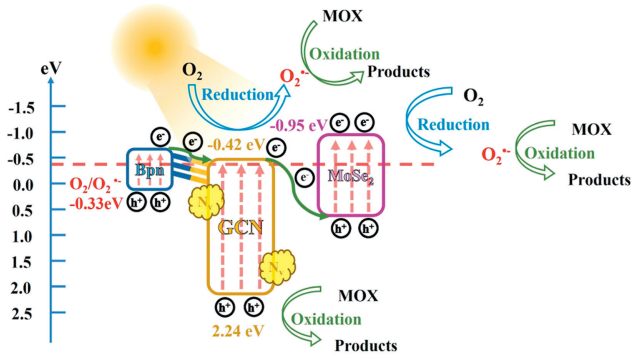

Fig. 4. Schematic diagram of MOX degradation mechanism over MBG.

components generated during photocatalysis and the energy band structures of the three semiconductors, which are critical for understanding the photocatalytic mechanism of MBG.

Based on the aforementioned results, we have inferred the mechanism of photocatalytic degradation as illustrated in Fig. 4. Bpn and GCN are characterized as p-type and n-type semiconductors, respectively, resulting in the rearrangement of energy band positions to form p-n junctions [50,46]. The narrow band gap of Bpn facilitates the excitation of electrons upon light exposure, causing them to transfer rapidly to the CB of GCN through the covalent bond between P and N atoms. This process leads to the reduction of oxygen in water, generating $O_2^{\bullet-}$ and facilitating the MOX degradation. Furthermore, the formed Z-scheme heterojunction between GCN and $MoSe_2$ allows photoinduced electrons to migrate to the VB of $MoSe_2$ and recombine with h^+, leaving the photogenerated electrons in the CB of $MoSe_2$ for the reduction of O_2 to produce $O_2^{\bullet-}$ (−0.33 eV). N-vacancies also serve as electron traps to enhance the separation of the photogenerated carriers on the GCN surface [41,51], leading to the oxidation of adsorbed MOX by h^+ in the VB of GCN.

Finally, the possible intermediates during the photocatalytic degradation of MOX were analyzed by a liquid chromatograph-mass spectrometer (LC-MS). Based on the identified intermediates (Figs. S8-S13 in Supporting information), two possible pathways are proposed (Fig. S14 in Supporting information). Pathway I: Under the reaction of $O_2^{\bullet-}$ in solution, the fluorine of MOX is replaced with −OH, and $O_2^{\bullet-}$ adds hydrogen to the piperazine ring to form **P1**. Finally, theses intermediates are mineralized into small molecular substances, CO_2 and H_2O. Pathway II: Hydroxyl addition occurs on the piperazine ring, generating **P2**. Following deacidification, cleavage, removal of cyclopropane from the naphthalene ring, as well as decarbonylation and dimethoxy reactions, **P3** is formed. By cleavage of the piperazine ring, **P2** is converted into **P4**, which further converts to **P5**. These intermediates are further decomposed into **P6** and eventually result in mineralization of small molecules, CO_2 and H_2O.

In summary, ternary heterojunctions of MBG containing p-n junctions and Z-schemes were successfully synthesized. Among MBG, Bpn and GCN are connected through the covalent bond between P and N atoms, which facilitates the transfer of photogenerated electrons from Bpn to the CB of GCN. Meanwhile, the Z-scheme heterojunction between $MoSe_2$ and GCN inhibits the recombination of photogenerated carriers. As expected, MBG exhibits an impressive removal of over 98% for MOX within 20 min under visible light irradiation, with a rate constant of 6.3 times higher than that of the pristine GCN. In addition, $O_2^{\bullet-}$ produced by photogenerated electron reduction is identified as the primary photocatalytic active species responsible for MOX degradation. This research holds significant potential for the advancement of efficient heterojunctions in photocatalysis through covalently bonded bridging.

Declaration of competing interest

The authors declare that they have no known competing financial interests or personal relationships that could have appeared to influence the work reported in this paper.

Acknowledgments

This study was financially supported by the National Natural Science Foundation of China (No. 52100076), the Fundamental Research Funds for the Central Universities (No. 2023MS064).

Supplementary materials

Supplementary material associated with this article can be found, in the online version, at doi:10.1016/j.cclet.2023.109453.

References

[1] M.C. Danner, A. Robertson, V. Behrends, J. Reiss, Sci. Total Environ. 664 (2019) 793–804.
[2] P. Kovalakova, L. Cizmas, T.J. McDonald, et al., Chemosphere 251 (2020) 126351.
[3] X. Van Doorslaer, K. Demeestere, P.M. Heynderickx, et al., Appl. Catal. B 138-139 (2013) 333–341.
[4] S. Li, T. Huang, P. Du, W. Liu, J. Hu, Water Res. 185 (2020) 116286.
[5] B. Zhou, L. Chen, F. Li, et al., Chin. Chem. Lett. 34 (2023) 108558.
[6] A.S. Oberoi, Y. Jia, H. Zhang, et al., Environ. Sci. Technol. 53 (2019) 7234–7264.
[7] C.M. Manaia, J. Rocha, N. Scaccia, et al., Environ. Int. 115 (2018) 312–324.
[8] D. Kanakaraju, B.D. Glass, M. Oelgemöller, J. Environ. Manage. 219 (2018) 189–207.
[9] W. Zheng, S. You, Z. Chen, et al., Environ. Sci. Technol. 57 (2023) 10127–10134.
[10] L. Jin, X. Duan, M. Sun, et al., ACS Nano 17 (2023) 12875–12883.
[11] M. Yu, H. Liang, R. Zhan, et al., Chin. Chem. Lett. 32 (2021) 2155–2158.
[12] D. Xu, Y. Ma, J. Wang, et al., Chem. Eng. J. 426 (2021) 131246.
[13] L. Jin, M. Sun, J. Yang, et al., Appl. Catal. B 339 (2023) 123150.
[14] X. Li, W. Luo, K. Zhu, et al., Chem. Eng. J. 474 (2023) 146016.
[15] W. Liu, Y. Li, F. Liu, et al., Water Res. 151 (2019) 8–19.
[16] B. Yang, J. Zhao, W. Yang, et al., J. Colloid Interface Sci. 589 (2021) 179–186.
[17] A. Balakrishnan, M. Chinthala, Chemosphere 297 (2022) 134190.
[18] Y. Zhou, M. Yu, H. Liang, et al., Appl. Catal. B 291 (2021) 120105.
[19] J. Qi, X. Yang, P.Y. Pan, et al., Environ. Sci. Technol. 56 (2022) 5200–5212.
[20] Z. Gan, C. Huang, Y. Shen, et al., Chin. Chem. Lett. 31 (2020) 513–516.
[21] J. Liu, S. Zhu, B. Wang, et al., Chin. Chem. Lett. 34 (2023) 107749.
[22] X. Ma, Y. Wei, Z. Wei, et al., J. Colloid Interface Sci. 508 (2017) 274–281.
[23] Y. Li, M. Zhou, B. Cheng, et al., J. Mater. Sci. Technol. 56 (2020) 1–17.
[24] D. Zhang, J. Qi, H. Ji, et al., Chem. Eng. J. 400 (2020) 125918.
[25] Y. Cheng, J. Zhang, X. Xiong, et al., J. Alloys Compd. 870 (2021) 159540.
[26] K. Zhu, W. Qin, Y. Gan, et al., Chem. Eng. J. 470 (2023) 144190.
[27] D. Zeng, P. Wu, W.J. Ong, et al., Appl. Catal. B 233 (2018) 26–34.
[28] D. Li, H. Wang, H. Tang, et al., ACS Sustain. Chem. Eng. 7 (2019) 8466–8474.
[29] H. Tang, K. Dou, C.C. Kaun, et al., J. Mater. Chem. A 2 (2014) 360–364.
[30] H. Zhang, G. Tang, X. Wan, et al., Appl. Surf. Sci. 530 (2020) 147234.
[31] L. Shi, Y. Wang, Y. Yan, et al., J. Colloid Interface Sci. 627 (2022) 969–977.
[32] J. Luo, F. Wang, J. Wan, et al., Clin. Chim. Acta 483 (2018) 216–221.
[33] T. Song, L. Hou, B. Long, et al., J. Colloid Interface Sci. 584 (2021) 474–483.
[34] H. Liu, Z.X. Liu, S. Wang, et al., Adv. Energy Mater. 9 (2019) 1900887.
[35] P. Schulz, L.L. Kelly, P. Winget, et al., Adv. Funct. Mater. 24 (2014) 7381–7389.
[36] X. Zhao, Y. You, S. Huang, et al., Appl. Catal. B 278 (2020) 119251.
[37] X. Zhang, R. Zhang, S. Niu, et al., Appl. Surf. Sci. 475 (2019) 355–362.
[38] L. Jia, X. Sun, Y. Jiang, et al., Adv. Funct. Mater. 25 (2015) 1814–1820.
[39] J. Ge, L. Zhang, J. Xu, et al., Chin. Chem. Lett. 31 (2020) 792–796.
[40] S. Zhou, Y. Wang, K. Zhou, et al., Chin. Chem. Lett. 32 (2021) 2179–2182.
[41] J. Cao, W. Nie, L. Huang, et al., Appl. Catal. B 241 (2019) 18–27.
[42] G. Zhang, M. Liu, T. Heil, et al., Angew. Chem. 131 (2019) 15092–15096.
[43] H. Liang, M. Yu, J. Guo, et al., Sep. Purif. Technol. 272 (2021) 118891.
[44] Y. Wang, L. Rao, P. Wang, et al., Appl. Catal. B 262 (2020) 118308.
[45] C. Lv, Y. Qian, C. Yan, et al., Angew. Chem. 130 (2018) 10403–10407.
[46] J. Wang, J. Ma, Q. Zhang, et al., Appl. Catal. B 285 (2021) 119781.
[47] G. Yang, P. Qiu, J. Xiong, et al., Chin. Chem. Lett. 33 (2022) 3709–3712.
[48] R. Guo, J. Wang, Z. Bi, et al., Chemosphere 295 (2022) 133834.
[49] L. Chen, J. Duan, P. Du, et al., Water Res. 221 (2022) 118747.
[50] W. Xue, H. Sun, X. Hu, et al., Chin. J. Catal. 43 (2022) 234–245.
[51] P. Yan, J. Dong, Z. Mo, et al., Biosens. Bioelectron. 148 (2020) 111802.